

Noninvasive manipulation of cell adhesion for cell harvesting with piezoelectric composite film

Xingyi Wan^{a,b}, Xiaodi Zhang^a, Zhirong Liu^{a,b}, Jiaming Zhang^{a,b}, Zhou Li^{a,b},
Zhong Lin Wang^{a,b,c,*}, Linlin Li^{a,b,*}

^a Beijing Institute of Nanoenergy and Nanosystems, Chinese Academy for Sciences, Beijing 101400, P.R.China

^b School of Nanoscience and Technology, University of Chinese Academy of Sciences, Beijing 100049, P.R.China

^c School of Materials Science and Engineering, Georgia Institute of Technology, Atlanta, GA 30332-0245, USA

ARTICLE INFO

Article history:

Received 21 June 2021

Revised 14 September 2021

Accepted 3 October 2021

Keywords:

piezoelectric effect
polyvinylidene fluoride/barium titanate
ultrasound
protein adsorption
cell harvesting

ABSTRACT

Cell sheet harvesting has recently emerged as a promising strategy for scaffold-free cell transplantation and tissue engineering. It is critical to achieve the disconnection between cell and its adherent support while maintaining the availability of cell sheet. Hence, the regulation of cell adhesion behavior often becomes the primary consideration for designing biomaterials used for cell sheet harvesting. The stimuli-responsive biomaterials can rationally modulate cell behaviors, especially adhesion performance. However, modulation of cell adhesion through noninvasive and highly efficient method is still greatly needed. Herein, a noninvasive low-intensity ultrasound-mediated cell harvesting is demonstrated based on the piezoelectric effect of polyvinylidene fluoride (PVDF)/barium titanate (BaTiO₃, BTO) composite film with superior electromechanical conversion ability. We found that the piezoelectric effect triggered by ultrasound (US) can modulate the absorption and secondary structure of adhesive protein fibronectin (FN) on the composite film, which further influenced cell adhesion force to finally obtain free-standing cell sheets. The detached cell sheets with accurate control retained their viability and excellent proliferative capability. These findings highlight the ability of the piezoelectric biomaterials for cell sheet engineering to serve as a noninvasive and accurately controllable platform via regulating surface protein adsorption and conformation, which indicates great application prospect of this piezoelectricity-based cell harvesting method in regenerative medicine.

© 2021 Elsevier Ltd. All rights reserved.

1. Introduction

Enlightened by the physicochemical properties of natural extracellular matrix (ECM), designing of biomimetic materials that can reproduce the unique properties of ECM has become one of the most attractive strategies for regulating cell behaviors and even directing cell fate [1–4]. Among different applications of these biomaterials, harvesting of functional cells, cell aggregates or cell sheets have attracted great interest for their applications in cell-based therapy [5]. This free-standing cell monolayer can be transplanted directly or integrated into tissue-like construction to the defective sites for simplifying the operation and avoiding cell loss [6–8], which have potential applications in wound healing [9], cell therapy [10], tissue regeneration [11], and bio-actuator [12]. An effective cell harvesting method largely depends on the pre-

cise modulation of cell detachment from the supports. Recently, stimuli-responsive biomaterials that possess the switchable physiochemical properties in response to external stimulations have been developed to regulate cell adhesion behavior [13–15]. For example, a potential-responsive self-assembled monolayer was reported to reversibly regulate cell attachment via switching the exposure of RGD peptide that is responsible for cell adhesion [2]. Poly(3,4-ethylenedioxythiophene) (PEDOT) with photothermal conversion ability was investigated to harvest intact cell monolayer via heat-induced decomposition of the collagen between the cells and the PEDOT [16,17]. Other tunable platforms that have been exploited for cell harvesting include magnet-responsive composites [11,18], photo/electro-cleavable chemical bonds modification [19,20], and ion regulation to either promote or suppress cell adhesion, etc [9]. However, most of these methods have cumbersome procedure, need repeated stimulation to achieve the overall cell harvesting, or/and have high cell damage during the manipulation process [21]. Recently, it has been reported that the electrical potential can regulate the conformation of cell adhesive proteins and

* Corresponding authors.

E-mail addresses: zhong.wang@mse.gatech.edu.cn (Z.L. Wang),
lilinlin@binn.cas.cn (L. Li).

ultimately lead to the disconnection of cell-material interaction to obtain cell sheets [19,22,23]. Nonetheless, these electrical signals are generally transmitted to the interface through electrical stimulators with additional wires and power supply, which may induce unwanted cell damage and great inconvenience [24,25].

Piezoelectric materials, including natural components such as collagen, deoxyribonucleic acids (DNA), and bone tissue [26], have non-centrosymmetric structures, which bring forth their unique piezoelectric property of accumulating electrical charges under applied mechanical force or deformation [27]. The unique stimulative piezoelectric biomaterials have recently attracted extensive attention and been widely applied in biosensors [28], actuators [29], diagnosis [30], and noninvasive biological electrostimulation [31–33]. Owing to the mechano-electrical conversion capability, piezoelectric materials can realize noninvasive in-situ electrostimulation under internal or external mechanical stress [31,34]. Moreover, it was found that the surface charge of piezoelectric materials can affect the adsorption behavior of proteins [35]. These findings inspire us that the surface piezoelectricity of piezoelectric biomaterials might be locally transduced to the cell-biomaterial interface, through which noninvasive in-situ regulation of cell adhesion can be realized to overcome the shortcoming of current wired electrostimulation and finally obtain continuous cell sheet.

In this work, we have fabricated piezoelectric PVDF/BaTiO₃ composite film with remarkable mechano-electrical performance and developed an innovative method for modulation of cell adhesion and cell harvesting. The addition of BaTiO₃, a promising multifunctional nanomaterials in biomedicine [36], endowed the PVDF with enhanced piezoelectricity. Under the remote and noninvasive ultrasound (US)-induced mechanical stimulation, the piezoelectric signal generated at the interface of the films/cells can regulate the adsorption and protein secondary structure of adhesive protein fibronectin (FN), which further modulated the cell adhesion force. Based on this mechanism, targeted and precision-controlled cell detachment is obtained for harvesting free-standing cell sheets of two different cell lines.

2. Materials and methods

2.1. Fabrication of PVDF and PVDF/BTO films

The BaTiO₃ nanoparticles were synthesized by a hydrothermal method. Briefly, 18 mmol Ba(OH)₂•8H₂O (98%, Aladdin) and 2 mmol TiO₂ (Aladdin) were dissolved in 5 mL deionized water and heated in a Teflon-autoclave at 200°C for 5 days. The final products were washed in hydrochloride acid, ethanol and deionized water successively until the pH value was 7 and dried at 60°C overnight. For preparation of PVDF film, 0.5 g PVDF (5.34 × 10⁵ Da, Aldrich) was dispersed in 5 mL N, N-dimethylformamide (DMF, Macklin) and stirred for 30 min. For preparation of BTO doped composite films, PVDF and BTO powders with different weight ratio were blended in 5 mL of DMF. Then the suspension was homogenized through robust stirring after sonication for at least 30 min. All films were fabricated by casting 400 μL solution on round glass slides (2 cm in diameter) and annealing at 40°C for 4 h to remove the solvent. For cell culture, all films were cut into right size pieces suited in the 24-well plate.

2.2. Characterization of nanoparticles and films

The phase structure of BTO NPs and the crystallinity of the films were determined by X-ray diffractometry (XRD, PANalytical Ltd., Netherland) with Cu Kα radiation (λ=1.5406 Å, 2θ=10°–80°). Morphological feature of BTO NPs and the films was characterized with scanning electron microscopy (SEM SU8020, Hitachi, Japan) by applying a 10 kV acceleration and an 80 pA current. Prior to imag-

ing, the samples were gold sputtered under 40 mA for 20 s. Microstructures of BTO were observed by a transmission electron microscopy (TEM) and a field-emission high-resolution transmission electron microscopy (HRTEM, 2100F). Fourier transform infrared (FTIR) spectra was performed on Veraex80V (Bruner Corp., USA) within the range of 400–2000 cm⁻¹. The proportion of β phase can be calculated by the Equation (1).

$$F(\beta) = \frac{A_{\beta}}{\left(\frac{K_{\alpha}}{K_{\beta}}\right)A_{\alpha} + A_{\beta}} \quad (1)$$

where A_{α} and A_{β} represent the absorbance at 763 cm⁻¹ and 840 cm⁻¹, respectively. And K_{α} and K_{β} represent the absorption coefficients at these two wavenumbers, of which the values are 6.1 × 10⁴ and 7.7 × 10⁴ cm² mol⁻¹, respectively [37]. The surface roughness of films was determined with a surface roughness tester (MarSurf, XCR20, Germany), n=5 for each group.

2.3. Electrical properties

Aluminum (Al) electrodes with a thickness of 500 nm were sputtered on both sides of the PVDF and PVDF/BTO films via magnetron sputtering. After that, the samples were polarized under conditions of 90°C, 4 kV for 60 min. Ferroelectric property was characterized via a commercial ferroelectric test setup (RTI-MultiFerroic, USA) with maximum field amplitude of 4 kV mm⁻¹ at a frequency of 1 Hz. The electrical outputs were recorded by an electrometer system (Keithley 6514). A linear motor with motive hammer was employed to generate periodical pressure while a commercial ultrasound transducer (Chattanooga Co., USA) was used to generate ultrasound at frequency of 1 MHz. Before measurements, the Al-coated films were encapsulated in Kapton tape to isolate the Al electrode from air and liquid. Zetasizer Nano ZS instrument (ZEN3600, Malvern Instruments Ltd, UK) was used to measure the surface potential of the films. The resultant mean value of surface potential was calculated from three parallel samples. Piezoelectricity of the PVDF and PVDF/BTO films was characterized by PFM (MFP-3D, Asylum Research) using a contact mode. The piezoelectric coefficients (d_{33}) of the films were evaluated by the piezoelectric coefficient meter (ZJ-3AN).

2.4. Bulk properties

The bulk property of films was investigated with extensometry by using a dual column universal testing machine (Instron EP3000, USA). Film thickness was measured in advance by a thickness tester (CH-10-A, Grows, Shanghai). For uniaxial tensile tests, the films were cut into 20 mm × 8 mm strips and loaded on the clamps. Displacement was applied with the rate of 2 mm min⁻¹.

2.5. Surface pre-treatment

All the films were treated with oxygen plasma for realizing a hydrophilic surface under the following conditions: 100 W; 0.8 mbar; gas flow of 50 sccm O₂; 2 min for each group. The distance from the plasma glow to the sample surface was 10 cm. Water contact angle of the films was tested by the contact angle measurement (XG-CAMB1, XUANYI). For surface coating of adhesion protein, the films were immersed in fibronectin dissolved in phosphate buffer saline (PBS) for 24 h at 37°C. After rinsing three times with PBS to remove the unassociated proteins, the level of protein adsorption was quantified using the bicinchoninic acid (BCA) protein kit (Beyotime, Shanghai). The structural information of the adsorbed protein was obtained by a circular dichroism (CD) spectropolarimeter (JASCO, J-1500, Japan) within the range from 190 nm to 250 nm. Quantitative analysis of the secondary structure

of FN was conducted using the Bestsel tool (<http://bestsel.elte.hu>) [38,39].

2.6. Cell isolation and culture

Adult rats (Wistar, male, 4 weeks old) were purchased from Vital River Company. The whole procedures for handling the animals firmly stick to the “Beijing Administration Rule of Laboratory Animals” and the national standards “Laboratory Animal Requirements of Environment and Housing Facilities (GB 14925-2001)”. Rat bone mesenchymal stem cells (rbMSCs) were obtained from femurs and tibias of rats according to our previous reports [40,41]. The purified cells were then seeded on the TCP in low-glucose Dulbecco's modified Eagle medium (1.0 g L^{-1}) (DMEM, Gibco) supplemented with 10% fetal bovine serum (Gibco) and 1% penicillin/streptomycin (Gibco). The rbMSCs were passaged when the cell density reached 70–80% of the dish area. The cells in four passages were used for the following experiments. NIH3T3 mouse fibroblasts were purchased from American Type Culture Collection and cultured in high-glucose DMEM (4.5 g L^{-1} , Gibco) supplemented with 10% fetal bovine serum (Gibco) and 1% penicillin/streptomycin (Gibco). All the cells were cultured at 37°C in a humidified incubator with 5% CO_2 . The culture medium was refreshed every 48 hours.

2.7. Biocompatibility and cell proliferation

All the samples were cut into round shape with diameter of 1 cm to fit the size of 24-well culture plate. Then, they were sterilized in 75% alcohol for 30 min, followed by the ultraviolet irradiation for 1 h on two sides of the films, respectively. A cell counting kit-8 assay (CCK-8, Dojindo Molecular Technology) was used for evaluating biocompatibility and the effect on cell proliferation. The viability of rbMSCs at the 4th passage and NIH3T3 was assessed at the 1st, 3rd, and 5th day after culturing on the films ($n = 6$ for each group). After incubation for different times, the original media were replaced by the fresh DMEM containing 10% CCK-8 working solution. After 4 h incubation at 37°C , the final production of water-soluble formazan dye was evaluated at a wavelength of 450 nm by a microplate reader (BIO-RAD, iMark).

2.8. Morphology of cells on the films

The morphology of rbMSCs on different films were observed by SEM after gradient dehydration. In brief, cells seeded on different films were fixed with 2.5% glutaraldehyde for 30 min and immersed in a graded ethanol series (30%, 50%, 70%, 80%, 90%, 95%, and 100%) in sequence for 30 min, respectively. Then, the samples were dried in an oven, followed by gold sputtered before imaging via SEM.

2.9. Ultrasound-induced cell stimulation

Before stimulation, the influence of US on cell viability was conducted via CCK-8 assay to determine an optimal ultrasound condition. A series of parameters (power intensity: 0, 0.2, 0.4, 0.8, 1.2, 1.5, 1.8, and 2 W cm^{-2} ; duration: 0, 5, 10, 15, 20, 30, 60, and 90 s) were detected to determine their influence on cell viability. Upon the rbMSCs proliferated and spread to form a monolayer cell sheet on the films, US stimulation was applied at different power density ($0\text{--}1.0 \text{ W cm}^{-2}$) and lasted for 20 s using an ultrasound platform (Chattanooga Co., USA) at a constant frequency 1 MHz and 50% duty cycle. Similarly, the NIH3T3 cells were plated on different films and treated to detach via the same ultrasonic procedure. All the experiments were replicated in triplicate.

2.10. Cell adhesion force assessment

The adhesive force of cells before and after US stimulation was measured via a centrifugation assay in the 96-well plates [42]. Briefly, a certain number of targeted cells ($10000 \text{ cells cm}^{-2}$) were seeded on the FN-coated films and the percentage of cells remained on the surface of the films under different centrifugal speed was utilized to calculate the cell adhesion forces. Calcein-AM was used to label live cells for determining the cell number before and after ultrasound treatment. After 1 d of culture to form a cell monolayer, the number of the cells attached on the film surface without any stimulation was measured as a total number basically. Next, the piezoelectric films were exposed to ultrasound beneath for 20 s with different intensities. Then, the 96-well plates containing the films were upturned and centrifuged at different speeds of 1000, 2000 and 3000 rpm (corresponding g value was 101, 406, and 915 cm s^{-2} , respectively) for 5 min. Ultimately, the number of remaining cells was assessed to quantify cell adhesion force.

2.11. Immunostaining

Immunofluorescent staining of cells was conducted as previously described [41]. Briefly, the confluent rbMSCs and NIH3T3 and the remaining cells before and after US-induced detachment were washed with PBS for three times, fixed with 4% paraformaldehyde for 20 min, extracted with 0.1% Triton X-100 (Sigma) for 10 min, and blocked with 10% goat serum for 1 h at room temperature (RT). F-actin cytoskeleton was stained with phalloidin-Alexa Fluor 488 (A12379, 1:200, Invitrogen) and phalloidin-Alexa Fluor 594 (A12381, 1:200, Invitrogen) for 4 h at RT for rbMSCs and NIH3T3, respectively. Cellular nuclei were stained with DAPI for 10 min before imaging. All fluorescence images were capture using a laser scanning confocal microscope (SP8, Leica). For identifying the effect of US-induced piezoelectricity on cell adhesion, the cells were immersed with the primary vinculin antibodies (mouse polyclonal, 1:200, Abcam) overnight at 4°C and then incubated with the Cy3-conjugated goat antimouse IgG secondary antibody (1:250, Beyotime) for 4 h at RT.

2.12. Cell sheet harvesting and viability assessment

After US stimulation, the cell sheets on the stimulating spot floating in the medium were transferred onto a new tissue culture plate (TCP) using tip-removed pipettes. The detached cell sheets were observed using an Olympus inverted research microscope (Olympus IX71, Japan) and immunostained to visualize F-actin and nuclei. The cell survival of the resultant cell sheets was determined via a live/dead assay and quantified by Image J software. Additionally, cell viability and proliferation were evaluated using a PicoGreen assay kit (P11496, Invitrogen) to quantify the double-stranded DNA (dsDNA) content following the manufacturer's instructions. Harvested cell sheets and cell suspension as control groups were cultured on TCP for 1, 2, 3, 4, and 5 days and lysed with lysis solution (0.1% Triton-100, 10 mM Tris-HCl, 1 mM ethylenediaminetetraacetic acid (EDTA), pH 7.5). The DNA content was determined by adding 1 mL of PicoGreen reagent into 1 mL of cell lysate ($n=3$). The mixed solution was incubated for 5 min in dark. The fluorescence of the samples was measured using a spectrofluorometer microplate reader (Victor X3, Perkin Elmer) at fluorescence wavelengths (excitation: $\sim 480 \text{ nm}$, emission: $\sim 520 \text{ nm}$). A standard curve was prepared using different concentration of DNA stock solution (1, 10, 100, 200, 500, 750, and 1000 ng ml^{-1}).

2.13. Statistics

All quantitative values shown in figures suggest the mean standard deviation (S.D.). The significant differences were determined

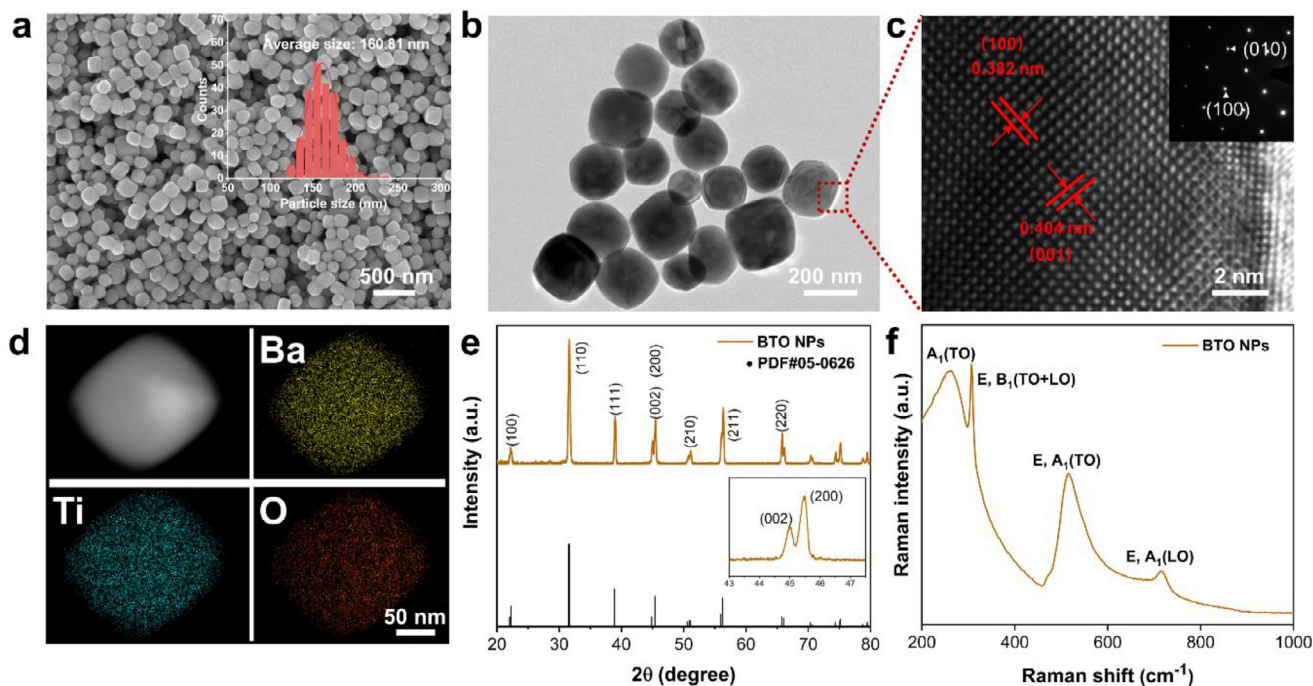


Fig. 1. Characterization of the tetragonal BTO NPs. (a) SEM image of BTO NPs. Insets show the size distribution of BTO NPs. (b) TEM image of BTO NPs. (c) HRTEM image and corresponding SAED of BTO NPs. (d) EDS mapping of Ba (yellow), Ti (blue), and O (red) element distribution in one BTO NP shown in the dark-field TEM image (top-left). (e) XRD pattern of BTO NPs and the enlarged (002, 200) characteristic peaks (inset). (f) Raman spectrum of the BTO NPs.

using one-way ANOVA. Statistical differences between groups of * $p < 0.1$, ** means $p < 0.05$, and *** represents $p < 0.01$ which indicates highly significant.

3. Results and discussion

3.1. Fabrication and characterization of PVDF/BTO films

The tetragonal BaTiO_3 nanoparticles (BTO NPs) synthesized via a one-step hydrothermal process had a near-cube structure with rounded edges, smooth surface, and even size distribution (Fig. 1a and b). Inset (Figure 1a) showed the average diameter was 160.81 ± 38.19 nm. The interplanar spacing from high-resolution TEM (HRTEM) image and selected area electron diffraction (SAED) were 0.382 nm and 0.404 nm, corresponding to the (100) and (001) plane, respectively. The subtle difference in crystal structural parameters confirmed the tetragonal symmetry of BTO NPs (Fig. 1c and inset). To visualize the distribution of elements and confirm the chemical component of BTO NPs, energy-dispersive spectrometer (EDS) elemental analysis of Ba, Ti and O was obtained. The EDS mapping showed that the three elements were uniformly distributed in the nanoparticle (Fig. 1d and S1). In the XRD pattern (Fig. 1e), there was a splitting peak at $2\theta = 44.8^\circ$ and 45.4° , which corresponded to the separated (002) and (200) diffractions of piezoelectric tetragonal crystalline phase (Fig. 1e and inset). Raman spectroscopy is another feasible approach to analyze the local distortions of the tetragonal-cubic symmetric structure of BTO NPs [43,44]. As shown in Fig. 1f, the predominant signals centered at near 250, 307, 515, and 715 cm^{-1} represented Raman scattering mode of the tetragonal BTO NPs. The characteristic peak at 715 cm^{-1} indicated an asymmetric vibration of $[\text{TiO}_6]$ octahedra, thus giving rise to the piezoelectricity of the synthesized BTO NPs [45].

3.2. Characterization of PVDF and PVDF/BTO composite film

A facile solution casting method was utilized to fabricate the PVDF and PVDF/BTO composite films (Fig. 2a) [46]. By adjusting

the content of the doped BTO NPs, a series of films with 0, 5, 10, 15 and 20 wt% BTO, denoted as PVDF, PVDF/BTO-5, PVDF/BTO-10, PVDF/BTO-15, and PVDF/BTO-20, respectively, were fabricated with a similar thickness of $\sim 50 \mu\text{m}$ (Fig. S2). When the mass fraction of BTO was no more than 15 wt%, the surface of all the films were relatively plain (Fig. S3a). However, it was observed that the overloaded BTO contents of 20 wt% induced shrinkage of the composite film and aggregation of the nanoparticles, which was not suitable for the following research (Fig. S3b). To enhance the piezoelectricity, electric poling treatment was carried out on the films [45]. From the SEM image of different PVDF/BTO composite films (Fig. 2b and S3a), the BTO NPs were uniformly dispersed in the PVDF matrix and no obvious nanoparticle aggregation or interfacial defects were observed. The addition of BTO NPs endowed the composite films with remarkable surface nanoroughness (Fig. 2c), which provides instructive topological information to guide cell attachment and growth [31,47]. The phase structure of different composite films were compared via XRD pattern and FTIR spectroscopy. Generally, PVDF contains five crystal phases, α , β , γ , δ and ϵ , among which β phase as the important crystalline contributes to the piezoelectricity [48]. In the XRD patterns (Fig. 2d), the typical peaks at 17.9° and 19.9° in the enlarged view were corresponding to α - and β - phase of PVDF, respectively. With the increase of BTO contents, the intensity of all the characteristic peaks of BTO especially the peak at $2\theta = 31.5^\circ$ increased accordingly, confirming the successful introduction of BTO NPs. Furthermore, in the FTIR spectra (Fig. 2e), the increase of BTO contents enhanced the β -phase percent of PVDF, which was reflected by the intensity of characteristic peak at 840 cm^{-1} and 763 cm^{-1} . The quantitative statistics of the polar phase content $F(\beta)$ and the crystallinity (X_c) further confirmed that the doping of BTO NPs could enhance both piezoelectric phase and crystallinity of PVDF (Fig. S4). A low BTO content in PVDF/BTO-5 did not significantly increase β -phase percent of PVDF (41.13%, compared with 39.06% of PVDF) and had relatively low crystallinity (58.4%, compared with 50.4% of pure PVDF). Optimally, 15 wt% BTO doping in PVDF/BTO-15 exhibited the highest proportion of β -phase that reached 92.48%. However,

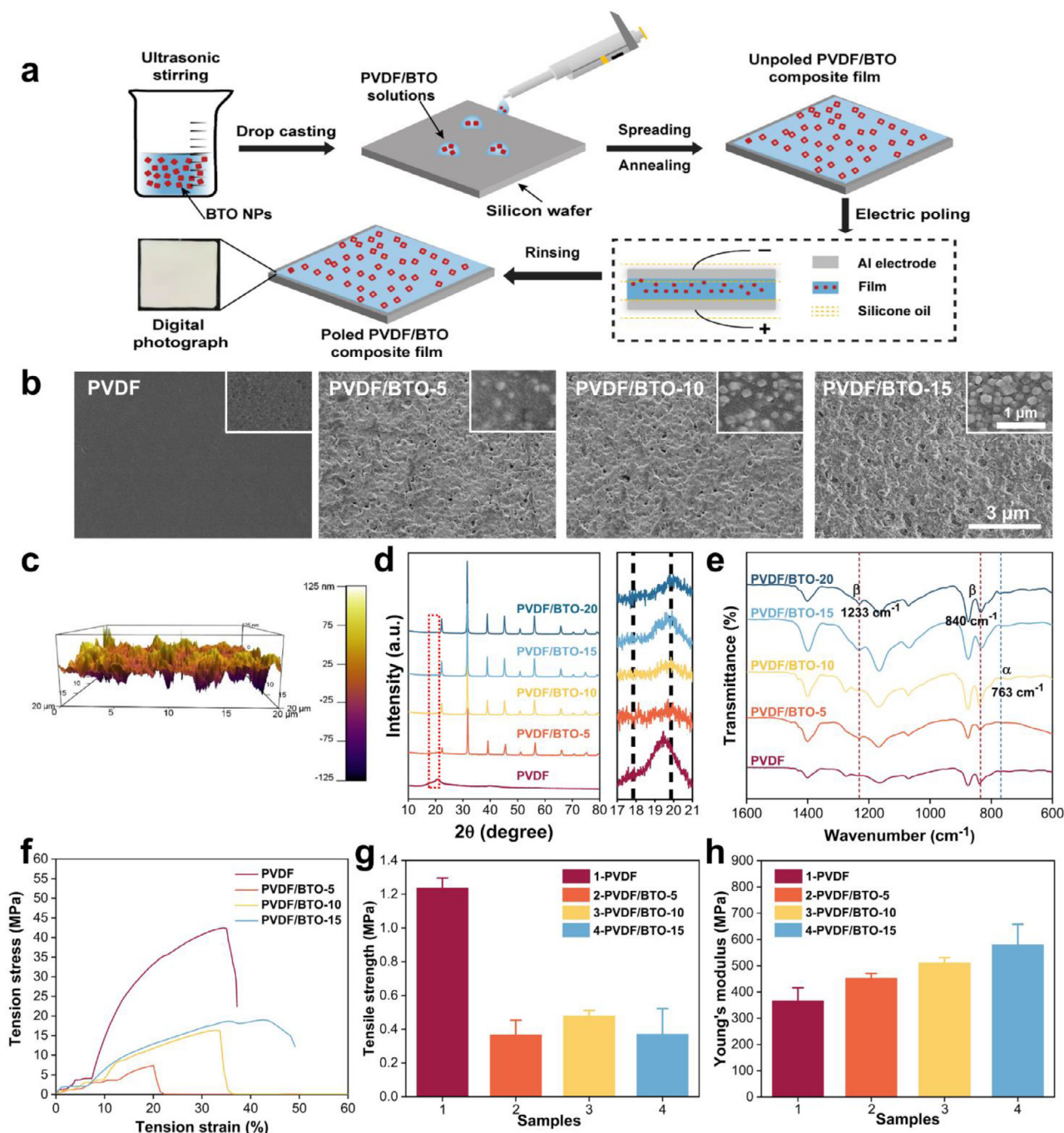


Fig. 2. Preparation and structural characterization of the PVDF/BTO composite films. (a) Schematic illustration for the fabrication of pure PVDF and PVDF/BTO composite films. (b) Representative SEM images of the composite films with different BTO contents of 0, 5, 10, and 15 wt%. Insets are the enlarged scanned images. (c) Three-dimensional AFM image of the PVDF/BTO-15 composite film. (d) X-Ray diffraction pattern of the films with different BTO contents and the enlarged region from 17° to 21° circled by the red line. (e) FTIR spectra of the films. The blue and red dash lines denote characteristic peaks of α and β phase of PVDF. Extensometry of PVDF/BTO composite films: (f) stress-strain curves, (g) tensile strength, and (h) Young's modulus.

20 wt% BTO induced a decreased β -phase content compared with the others (Fig. 2e, Fig. S4). It was suggested that the excessive nanoparticles interrupted the intrinsic structure of PVDF and hindered the crystal growth along the β -phase direction, thus causing an attenuated piezoelectric phase content [49].

Suitable mechanical properties of an objective material are highly needed to construct a support for maintaining normal cell behaviors. The stress-strain curve of the PVDF and PVDF/BTO composite films are presented in Fig. 2f, from which Young's modulus and tensile strength are calculated (Fig. 2g and h). The Young's

modulus of PVDF, PVDF/BTO-5, PVDF/BTO-10, and PVDF/BTO-15 films were 370 ± 30 MPa, 450 ± 78 MPa, 504 ± 83 MPa and 576 ± 103 MPa, respectively (Fig. 2h). It was deduced that BTO doping increased PVDF crystallinity and remarkably improved stiffness of the film. In addition, the break of the composite films was more likely to occur at a lower strain compared with PVDF film. These mechanical parameters jointly showed that the original mechanical properties of PVDF was completely changed in the presence of BTO NPs and a suitable doping content could optimize the capability of the materials to perceive mechanical stimulus and transmit

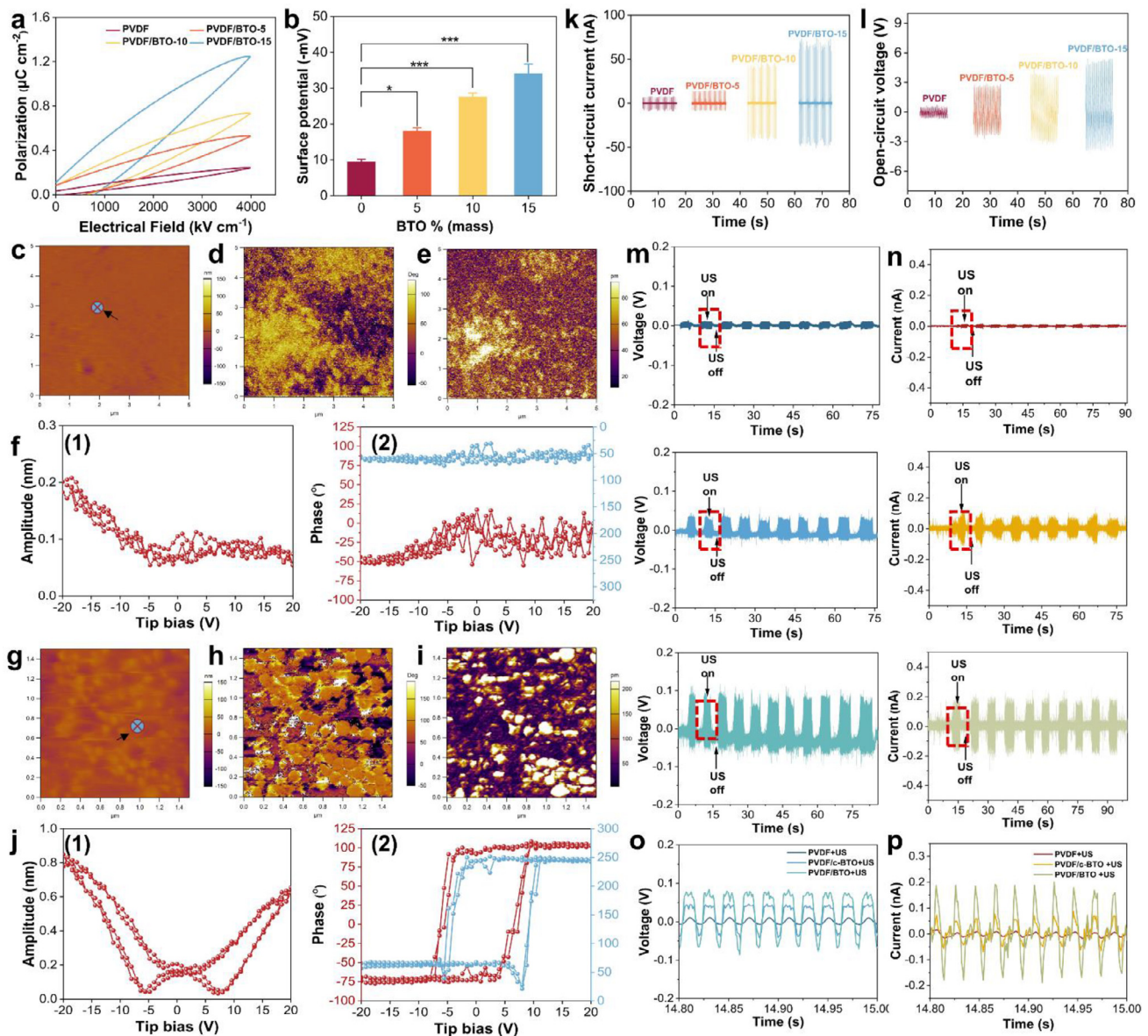


Fig. 3. Characterization of electrical properties of the films. (a) The hysteresis loops of the PVDF, PVDF/BTO-5, PVDF/BTO-10, and PVDF/BTO-15. (b) The surface potential of the films with increased contents of BTO NPs. Piezoresponse force microscopy maps and measurements of (c)-(f) PVDF and (g)-(j) PVDF/BTO-15 composite film. (c), (g) AFM topography of PVDF and PVDF/BTO-15. (d), (h) Amplitude images and (e), (i) phase images corresponding with the points of the black arrows in PVDF and PVDF/BTO-15 films, respectively. (f)-(1), (j)-(1) Amplitude, and (f)-(2), (j)-(2) phase hysteresis loops of PVDF and PVDF/BTO-15 films. Output performance of (k) short-circuit current and (l) open-circuit voltage of the composite films. (m, n) Ultrasound-induced piezoelectric output voltage and current of PVDF, PVDF/c-BTO and PVDF/BTO films and (o, p) the corresponding enlarged views of red dot circle.

an external strain thoroughly. Besides, the stiffness of the resultant composite films was much closer to that of ECM in cartilage or bone (100–1000 MPa), which would provide a desirable condition for the cells to growth and development [50].

3.3. Piezoelectric performance of PVDF/BTO composite film

We further detected the electrical properties of different films. Before electrical testing, all the samples were sputtered with aluminum electrodes on both side of the films, followed by an electrical poling treatment. In the hysteresis loops, after poling at the same condition, the residual polarization of the films increased with the increased contents of BTO NPs, indicating the enhanced polarization capability of the films responsive to an external electric field (Fig. 3a). Compared with PVDF film, the electrical polarization of the PVDF/BTO-15 film increased by nearly 6-folds, which

would further improve the ability of force-electric conversion of the film. The surface negative Zeta potential of the films gradually increased with increased BTO doping (Fig. 3b). Considering the nanometer size of BTO NPs, the surface area of the composite films was increased after BTO doping, which was in proportion to the solid-liquid interfacial polarization. Therefore, the surface potential of the PVDF/BTO composite films displayed an obviously increasing tendency with increased BTO NPs [51]. Macroscopically, the significantly augmented electrical polarization of the film was observed. These results suggested that the PVDF/BTO films had better piezoelectricity than the pure PVDF film and the best performance was achieved when the BTO NPs doping was 15 wt%.

This argument was further verified by piezoresponse force microscopy (PFM) as well as the electrical output of the two kinds of films (Fig. 3c-l). The atomic force microscope (AFM) topography, phase and amplitude images of both the pure PVDF and the

PVDF/BTO-15 were synchronously acquired by conducting PFM in a contact mode. The surface topographic images (Fig. 3c and g) exhibited distinct surface morphology and roughness of the two samples, in consistent with the SEM images. More significantly, phase curve and amplitude of the hysteresis loops, as a result of applying DC voltage from -20 V to +20 V, showed distinct piezoelectricity of these two kinds of films (Fig. 3d-e for PVDF, and h-i for PVDF/BTO). For the PVDF film, both phase curve and amplitude hysteresis loops indicated a low piezoelectricity (Fig. 3f). In contrast, the maximum amplitude of the PVDF/BTO-15 film reached 0.65 nm and 0.85 nm at the highest positive (+20 V) and negative tip bias (-20 V), respectively (Fig. 3j). The near 180° change of phase curve from -20 V to +20 V suggested a successful polarization switched triggered by the electric field. Piezoelectric coefficient (d_{33}), a direct index reflecting the linear coupling relationship between the mechanical and electrical properties of piezoelectric materials, was also evaluated (Fig. S5). It was found that the d_{33} value also increased with the increase of BTO content and reached the maximum of 15.7 pC N⁻¹ for PVDF/BTO-15. It indicated the enhanced piezoelectricity was due to the increased contents of BTO NPs.

For measuring the electrical output performance, the films were first cyclically stroked by a slidable hammer with a constant force (~15 N). As for the unpoled samples, the electric output performance was relatively unsatisfactory despite that the addition of BTO NPs increased the electric output to some degree, suggesting the necessity of electrical poling to enhance the piezoelectricity (Fig. S6). After the electrical poling, the PVDF/BTO composite films delivered much higher current and voltage output than that of PVDF film (Fig. 3k and l). Meanwhile, the increased BTO contents significantly improved the electric output and reached a maximum of 110 μ A and 9 V when the BTO content was 15 wt%. Considering the feasibility and practicability of US to activate the mechanical-electrical conversion of piezoelectric materials [32,45,52], the piezoelectric outputs under US stimulation were also conducted. To better illustrate the influence of doped tetragonal BTO NPs on piezoelectricity of PVDF matrix, the composite films doped with non-piezoelectric cubic BTO NPs (c-BTO), denoted as PVDF/c-BTO, were also prepared as a control. Under the same US condition (0.8 W cm⁻²), PVDF/BTO films showed the largest output voltage (~100 mV) and current (0.19 nA), which were 2.5 and 7.6 times of that of PVDF and PVDF/c-BTO films, respectively (Fig. 3m-p). Furthermore, signals from the PVDF/BTO films increased as the US intensity increased, exhibiting a potential ability to tailor the piezoelectric output by controlling the applied US (Fig. S7). These results suggested that the tetragonal BTO was essential for the high ultrasonic-driven piezoelectricity of the composite films.

3.4. Surface properties and protein absorption on the PVDF/BTO composite film

Based on the remarkable piezoelectricity and suitable mechanical properties, the PVDF/BTO-15 composite film was selected for further assay. It was shortened as PVDF/BTO as no other composite films were used in the following parts. The PVDF and PVDF/c-BTO film were set as the low-piezoelectric group, and non-piezoelectric polyvinyl chloride (PVC) film with similar chemical and surface properties was used as a negative control for discerning the dominant influence factors including surface roughness and piezoelectricity. Both the PVC and PVDF/c-BTO film showed a similar surface morphology as the PVDF and PVDF/BTO film (Fig. S8). Meanwhile, similar surface roughness of the PVDF/c-BTO and PVDF/BTO films could further exclude the influence of topological structure (Fig. 4a). Due to the intrinsic hydrophobicity, all the films were surface pre-treated with oxygen plasma to increase hydrophilicity for promoted cell adhesion. After treatment, the hydrophilicity was

efficiently enhanced and the water contact angle (WCA) was decreased from nearly 120° to about 75° for all the films (Fig. 4b). The similar WCA of the films ensured that when researching the influence of the films on cell attachment and spreading, the factor of surface energy could be excluded.

Given that the adsorbed protein on biomaterials can regulate cellular adhesive behaviors via affecting the cell interaction with ECM components, we studied the protein adsorption capacity of the films. As a major anchor protein of ECM, FN can mediate the early cell adhesion, which profoundly impacts on subsequent cell behavior including migration, spreading, proliferation and differentiation [53,54]. The adsorption and conformation of FN is critical for mediating the interaction between adherent cells and the supporting biomaterials. After the oxygen plasma treatment and a 24 h soaking in FN solution, the protein content on the PVDF/BTO films showed no obvious difference from PVDF/c-BTO, but was 2.0-fold and 1.3-fold of that of the pure PVDF and PVC film, respectively (Fig. 4b). It can be attributed to the increased roughness and the enhanced polarization of the PVDF/BTO composite film [51]. Meanwhile, the protein adsorption on the PVDF/BTO composite film decreased after the exposure of the film to US, while it remained unchanged for PVC, PVDF, and PVDF/c-BTO film at the same applied US (Fig. 4c). The attenuate protein adsorption level was also confirmed by the changed value of WCA (Fig. 4d). Compared with the low piezoelectricity samples, the hydrophobicity of the composite films increased regardless of BTO contents. To further investigate the surface property of the piezoelectric PVDF/BTO films under US stimulation, the surface potential of the films with different BTO contents was evaluated immediately after ultrasound. As shown in Fig. 4e, after US treatment (0.8 W cm⁻², 20 s), the surface electrical potential became more negative for the piezoelectric PVDF/BTO films when compared to the PVDF film. These results implied that the piezoelectric effect triggered by the US stimulation would influence the amount of FN adsorption on the composite film, thus regulating the surface properties to manipulate cell adhesive behavior. Given that the changes of FN conformation will change the binding affinity to cells and thus alternate the cell adhesion, we speculated that the piezo-responsive PVDF/BTO films would reconstruct the conformation of FN molecule under US stimulation [2,55,56]. It may affect cell adhesion behavior because the switchable surface hydrophilicity can reverse cell attachment through changing the adsorption of the adhesive proteins [57].

Circular dichroism (CD) was utilized to investigate the secondary structure of the FN molecule after US stimulation [38]. It was obvious that the intact FN had a typical β -sheet enriched spectrum. When FN was adsorbed on the PVDF/BTO films, there was a slight difference of peak intensity appeared at 195 nm and 205 nm. Upon US, the peak pattern of FN in the spectrum significantly changed (Fig. 4f). The quantitative analysis confirmed that the secondary structure of the protein responded to piezoelectricity-triggered change of material surface potential (Fig. 4g, Fig. S9 and S10). When being naturally adsorbed on the surface of the PVDF/BTO composite film, FN exhibited conformation enriching β -sheet. Upon US, the activated piezoelectricity from the PVDF/BTO film reduced β -sheet percent and the proportion of α -helix increased, whereas the FN structure had almost negligible change in the solution with US treatment. These results indicated that piezoelectric effect could interfere with the FN conformation. This conclusion was also consistent with a previous report that the interfacial interaction between the material and the adsorbed proteins influenced the β -sheet secondary structure [58]. Also, the conformation change of the adhesive protein has been reported to decrease the molecule deposition on the polyelectrolyte film, thus leading to the insufficient interaction between adhesive protein ligands and integrin receptors to ultimately weaken cell

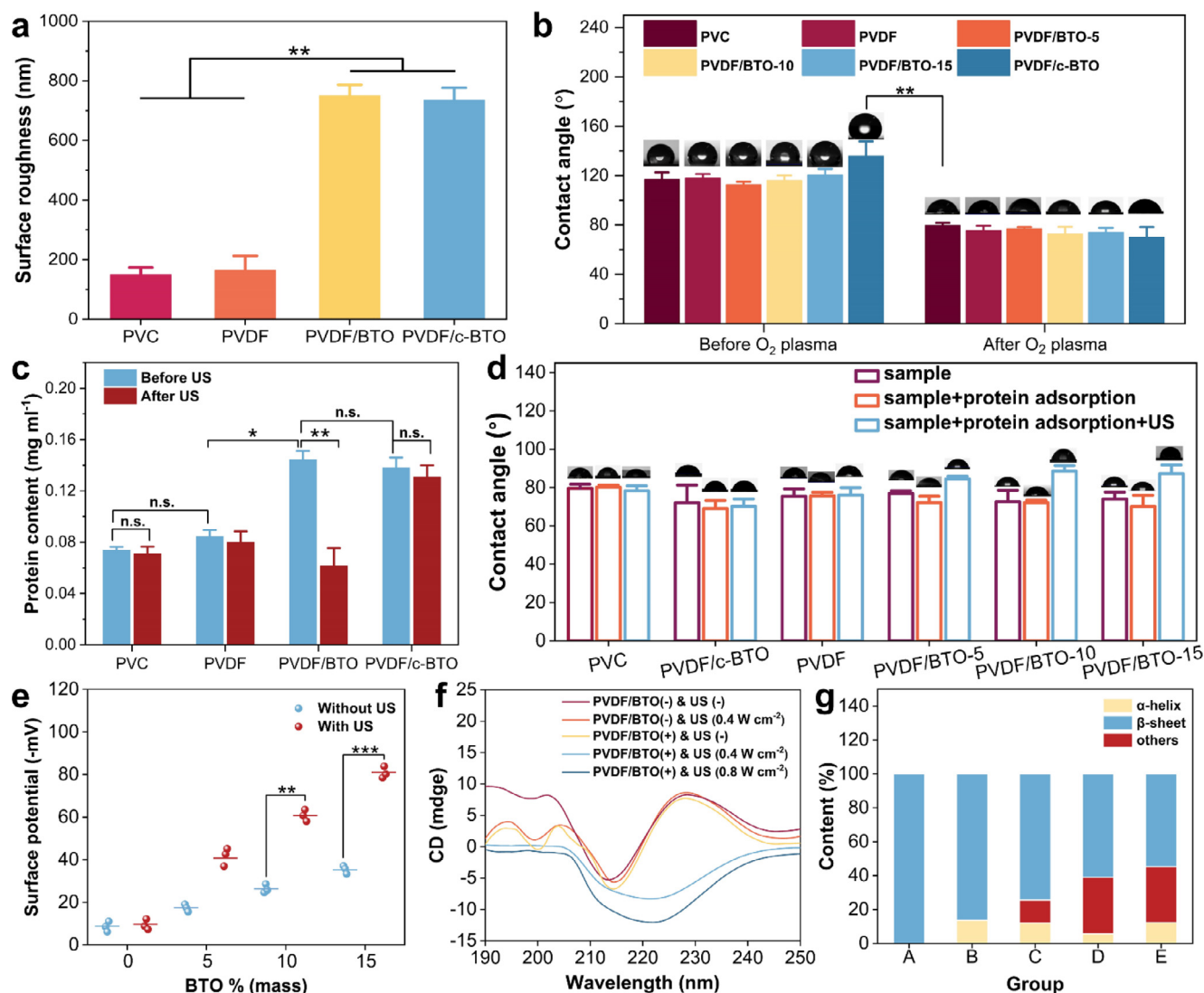


Fig. 4. Evaluation of the ultrasound-induced surface properties and alteration of FN conformation. (a) Surface roughness of different films. (b) Contact angles of different films before and after oxygen plasma treatment. (c) Quantitative statistic of protein content on the PVC, PVDF, PVDF/c-BTO and PVDF/BTO films before and after US. (d) Changes of contact angle upon ultrasound stimulation with and without FN adsorption. (e) Surface potential before and after US treatment. (f) CD spectra of FN protein coated on the PVDF/BTO films after different treatment with (0.4 or 0.8 W cm⁻², 20 s) or without ultrasound. (g) Main content of α -helix and β -sheet in different samples. (A: FN solution in PBS; B: FN adsorbed on the PVDF/BTO film without US stimulation; C: FN solution with US stimulation; D: FN adsorbed on the PVDF/BTO film with 0.4 W cm⁻² US stimulation; E: FN adsorbed on the PVDF/BTO film with 0.8 W cm⁻² US stimulation.

adhesion [59]. These results implied that the US-triggered piezoelectricity of the PVDF/BTO composite film weakened the interfacial protein interaction via changing the conformational structure of FN.

To precisely illustrate whether the piezo-potential activated by US was enough to activate the change of FN conformation, theoretical calculation was further conducted to determine the surface piezoelectric potential triggered by the US at 0.8 W cm⁻². The detailed calculation process was given in Supporting Information. The surface piezoelectric potential of the PVDF/BTO film could reach about -89.1 mV, which fitted well with the measured surface potential (Fig. 4d) and the US-driven output (Fig. 3m). It was sufficient for FN to undergo a structural change according to previous reports [22,60].

3.5. Biocompatibility and cell adhesion

CCK-8 assay was used to evaluate the biocompatibility of the applied US and the piezoelectric films on rbMSCs and NIH3T3

cells. Under US condition of power density ≤ 0.8 W cm⁻² and lasting time ≤ 20 s, cell viability was over 90%. Further increase of the power density and prolonging of time might induce decreased cell viability, which finally remained at about 70% (Fig. 5a). Thereby, we chose 0.8 W cm⁻² and 20 s as the maximum US condition for the following US-involved assays. Also, this US condition did not affect cell proliferation within 7 days (Figure 5b). After a 5-days culture, a similar proliferation rate of rbMSCs and NIH3T3 was observed on PVC, PVDF, PVDF/c-BTO and PVDF/BTO films (Fig. 5c), although proliferation rate on the PVDF/BTO film was slightly higher than the other groups. Live/dead assay also suggested a high biocompatibility of the four kinds of films (Fig. S11). The cell morphology observed from SEM directly reflected that the number of extended pseudopodia of rbMSCs on the PVC and PVDF films was quite few, mainly due to the lack of superficial micro-nano structure for the cells to anchor and attach (Fig. 5d, 1-2). Conversely, the cells elongated more and longer filopodia or protrusion on the PVDF/c-BTO and PVDF/BTO films (Fig. 5d, 3-4), which presented surface nanoroughness and offered more

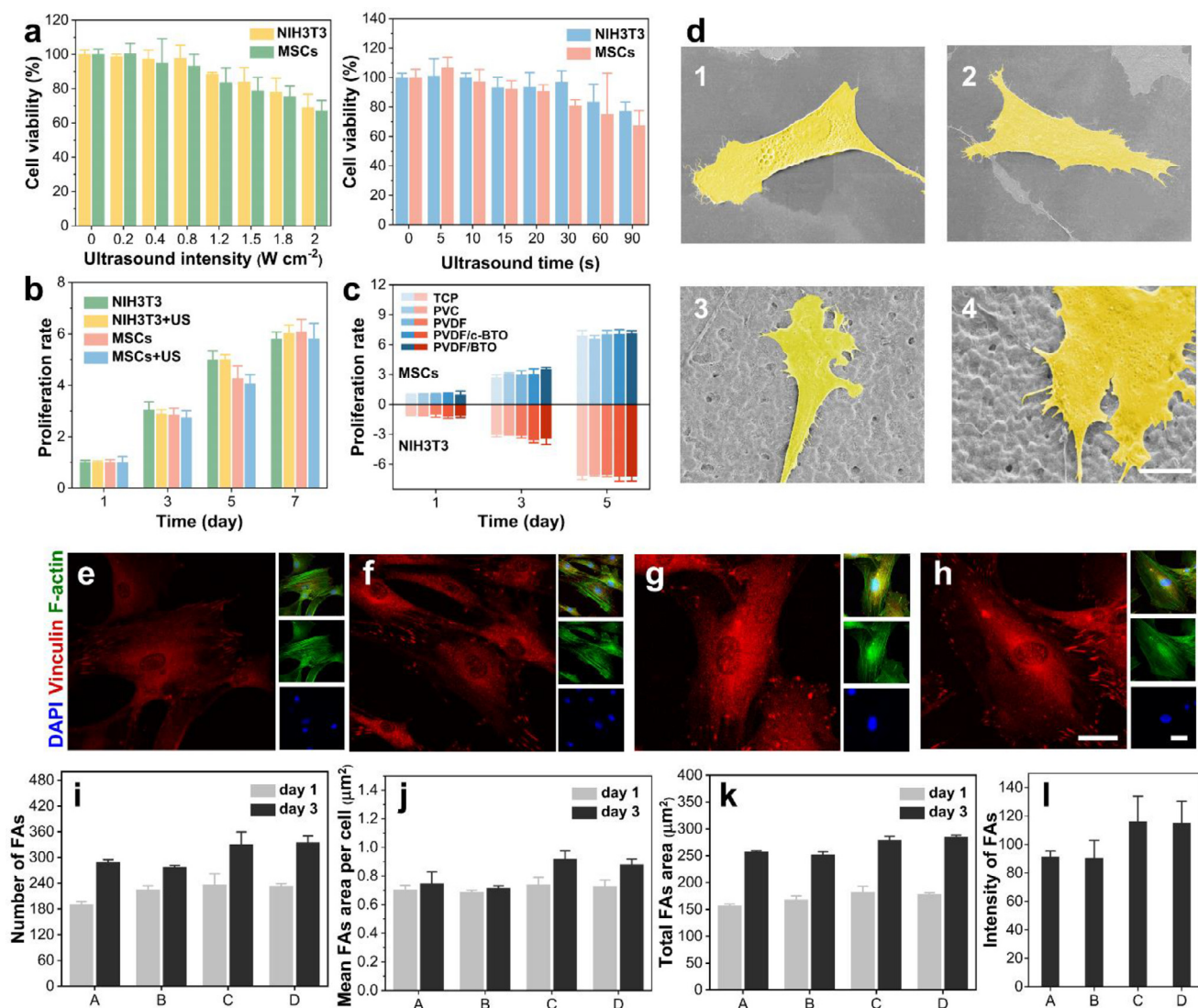


Fig. 5. Cytocompatibility and cell adhesion behavior. (a) Cell viability under different US conditions. (b) Cellular proliferation with or without US stimulation for 7 days (0.8 $W\text{ cm}^{-2}$, 20 s). (c) Histogram of the statistical results of the rbMSCs and NIH3T3 proliferation rate. Values are normalized against that grown for 1 day of the control group. (d) Representative SEM images of rbMSCs after culturing for 3 days on (1) PVC, (2) PVDF, (3) PVDF/c-BTO and (4) PVDF/BTO film. Scale bar = 20 μm . Immunostaining of rbMSCs on (e) PVC, (f) PVDF, (g) PVDF/c-BTO and (h) PVDF/BTO composite film. Cells were stained for F-actin cytoskeleton (green), vinculin (red), and nuclei (blue). Scale bar = 250 μm . The corresponding quantitative analysis of (i) the number of FAs, (j) mean FAs area per cell, (k) total FAs area on day 1 and day 3, and (l) mean fluorescence intensity of FAs on the films after incubation for 3 days. Data are presented as the mean \pm SD ($n = 5$). Group A, B, C, and D in (i)-(l) represent PVC, PVDF, PVDF/c-BTO and PVD/BTO films, respectively.

anchoring sites for cells to hold. The cellular stress fiber and focal adhesion (FA) distribution on different films were further investigated via immunofluorescent staining of filamentous actin (F-actin) cytoskeleton and vinculin expression (Fig. 5e-h), which might be further used to predict cellular mechanotransduction [61,62]. It was found that rbMSCs on the composite PVDF/c-BTO and PVDF/BTO films presented more regular stress fiber and remarkable ambient vinculin (Fig. 5g and h). Moreover, quantitative statistics of FAs within the first 24 h showed that rbMSCs on the composite films had enriched FAs. The FAs area per cell on the composite films was 1.26-1.27-fold of those on the PVC and PVDF films (Fig. 5i and j). After culturing for 3 days, the cells began to be connected with each other to form a confluent layer (Fig. S12), and no remarkable difference in total FA area was detected on different films (Fig. 5k), whereas higher intensity of FAs was observed on the composite films with larger surface roughness (Fig. 5l). These results provided instructions for distinguishing the function of piezoelectricity from surface properties on cell adhe-

sion, which proved the predominant role of piezoelectricity in cell detachment.

As being discussed above, the US-triggered piezoelectric effect can adjust the conformation of FN adsorbed on the PVDF/BTO film to a low-adhesive state, thus weakening the connection between the cells and the films. Thereby, to prove the US-induced film-FN-cell interfacial changes through piezoelectric effect, a centrifugation cell adhesion assay for both rbMSCs and NIH3T3 cells was conducted to measure cell detachment force before and after US stimulation [42]. The cell adhesion force was estimated through the proportion of residual cells relative to centrifugal forces after US. It was found that under a specific centrifugation speed, the cell adhesion force decreased after the US exposure of the FN-coated PVDF/BTO film (Fig. 6a). Moreover, increased intensity of US brought about the weaker cell adhesion force. Specifically, under a centrifugation speed of 3000 rpm, the adhesion forces of rbMSCs on PVDF/BTO were calculated to be 0.196, 0.120 and 0.081 nN without US, with 0.4 $W\text{ cm}^{-2}$ US, and 0.8 $W\text{ cm}^{-2}$ US treatment,

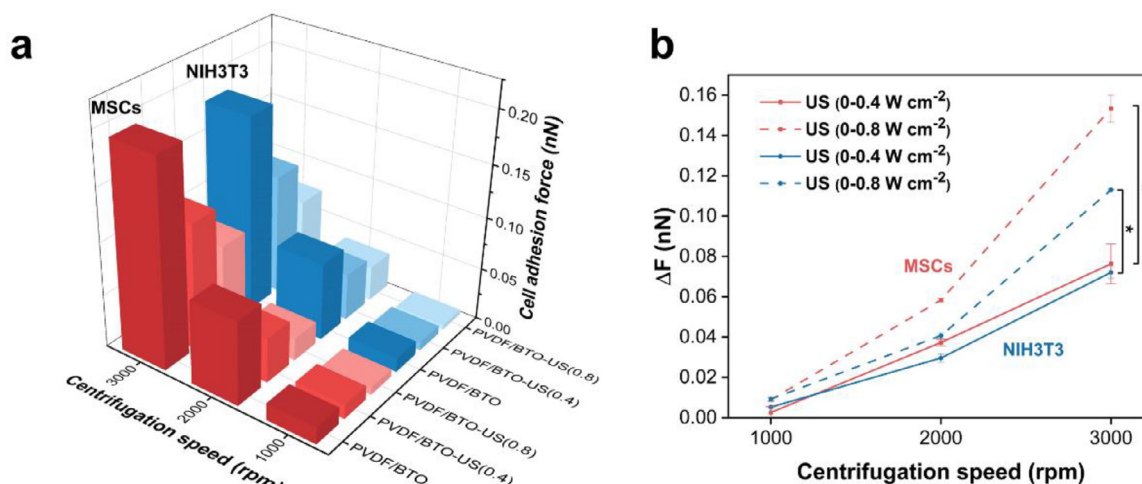


Fig. 6. Cell adhesion force of rbMSCs and NIH3T3 cells on the films. (a) Measured cell adhesion force of rbMSCs and NIH3T3 cells on the PVDF/BTO composite films before and after ultrasound (0.4; 0.8 W cm⁻²) via centrifugation cell adhesion assay. Cell adhesion force measured at 3 levels of centrifugal speeds: 1000, 2000, and 3000 rpm. (b) The difference of adhesive force (ΔF) quantified from a) before and after different intensities of ultrasound (0.4, 0.8 W cm⁻²). The legends of 0-0.4 W cm⁻² and 0-0.8 W cm⁻² represent the change of adhesion force on the surface of PVDF/BTO films at different centrifugal speeds under the 0.4 and 0.8 W cm⁻² ultrasound, respectively.

respectively (Fig. 6a). In comparison, rbMSCs on the PVDF/BTO with 0.4 and 0.8 W cm⁻² US had 36.8% and 58.7% decreased cell adhesion force, respectively, when compared to the US-free case (Fig. 6b). Consistently, similar results appeared when the centrifugal speeds were at 1000 and 2000 rpm and also for NIH3T3 cells (Fig. 6a). These results suggested that the US-induced piezoelectric effect could regulate the surface properties of the films and synergistically alter the FN conformation to weaken the cell-film interaction.

3.6. Cell harvesting upon ultrasound-induced piezoelectricity

To further realize cell detachment via the piezoelectric effect, a cell detachment assay was carried out. PVC, PVDF and PVDF/c-BTO were used as the negative controls. After 3 days of culture, rbMSCs on the piezoelectric PVDF/BTO films formed a confluent monolayer (Fig. S13). After US stimulation (0.8 W cm⁻², 20 s), rbMSCs rapidly separated from the PVDF/BTO film as a monolayer and a remaining cavity was visualized by fluorescence staining of the cells (Fig. 7a). The curled cells in the marginal region of the cavity were caused by the US stimulation and decreased cell adhesion force. The staining results showed that the F-actin and vinculin was only collapsed in the marginal region of the detached area. Cells away from the detachment region without US exposure still maintained intact morphology, further implying that the cell detachment was activated by the US-triggered piezoelectric effect. In contrast, under the same US condition, cells were still tightly attached on the low piezoelectric PVDF and PVDF/c-BTO, and the non-piezoelectric PVC films, as well as the normal tissue culture plate (TCP), respectively (Fig. S14). Similarly, this US-triggered cell detachment on the piezoelectric film was also applicable to NIH3T3 (Fig. S15). Thus, the distinct cellular response can be attributed to the high piezoelectricity of the PVDF/BTO nanocomposite films triggered by US.

The live/dead assay confirmed the viability of the cells on the composite films before and after US-induced detachment were both higher than 95%, indicating that this method did not cause obvious cell damage (Fig. 7b). Besides, the viability of the newly harvested cell sheets reached 92.7% and remained 94.8% after incubation in the medium for 2 h (Fig. 7b). Therefore, the US-triggered piezoelectric effect disrupted the linkage between films and the adhesive proteins responsible for cell adhesion, which ultimately achieved the harvesting and potential reuse of the detached cell aggregates (Fig. 7c).

The morphology of the harvested cell sheet of rbMSCs and NIH3T3 cells was further visualized via immunostaining. Images displayed connected cell cytoskeleton with structural stability and integrity (Fig. 7d). Interestingly, we noticed that the shape of the exfoliated cell aggregates did not match well with the size and shape of the ultrasonic probe, which might contribute to the heterogeneous distribution of the acoustic waves emitted from the probe.

Particularly, we found that with the increased ultrasound power density from 0.2 to 0.8 W cm⁻², an increasing area of rbMSCs was shed off in-situ from the surface of the PVDF/BTO film (Fig. S16). This tendency might be relative to the enhanced piezoelectricity under increased US intensity as the signal outputs were shown. The maximum cell detachment area can reach 53.7% of the total attached cell area under the US condition of 0.8 W cm⁻² for 20 s (Fig. 7e). Of note, US itself beyond a power density threshold might affect cells negatively. During the experiment, we noticed that the cell connection was inevitably interrupted accompanied by the disintegration of cell monolayer when 1 W cm⁻² US was imposed on cells for 20 s (Fig. S17 and S18). The phenomenon might account for the reason that the excessive US intensity might generate extra heat, and US cavitation and vibration became the predominant factors, whereas the mechanical-induced piezoelectric effect on the films was concealed, which was not expected in the experiment. Therefore, cooperative control of the ultrasound condition and properties of the piezoelectric film is essential to realize a desirable outcome.

In addition, the exfoliated rbMSCs and NIH3T3 sheet retained their proliferation capacity in a manner that was comparable to those on TCP control group within 5 days, as confirmed by a PicoGreen assay (Fig. 7f and g). The total content of DNA in the cell sheets significantly increased, which implied the increase of cell number. It is acknowledged that rbMSCs can serve as a feasible cell source for tissue regeneration and cell therapy due to their abundant sources [63,64]. Exploitation of novel pathways to harvest the cells with cell integrity and sustained activity are urgently required for practical applications. Therefore, the piezo-induced cell aggregate harvesting showed great potential in biomedical engineering and regenerative medicine. The rbMSCs and NIH3T3 cell sheets were stained via live/dead assay after additional short-term (2 h) and long-term (3 d) culture (Fig. S19 and S20). These results suggested that both kinds of the cell sheets maintained excellent viability once harvested immediately, and proliferation normally.

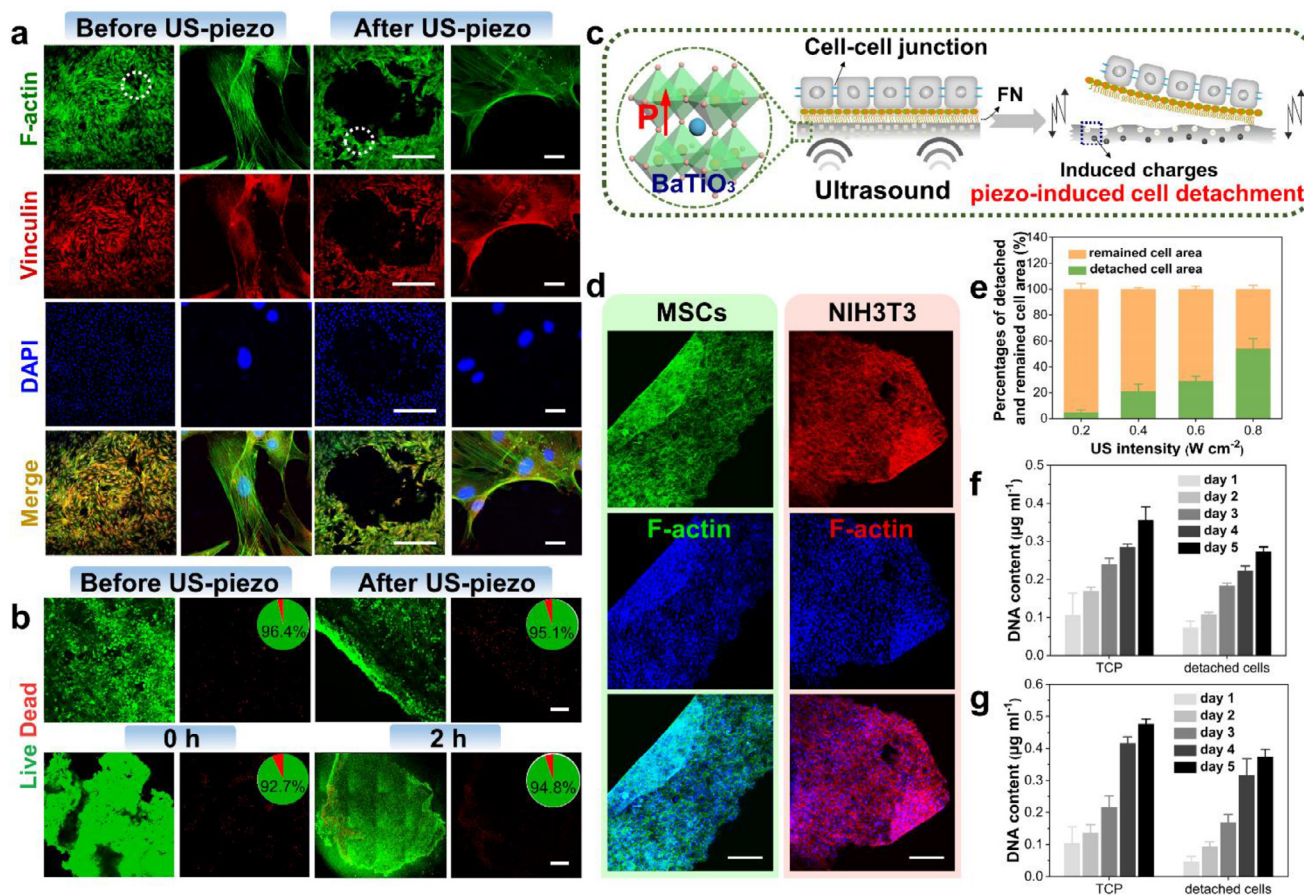


Fig. 7. Immunofluorescent images of remaining cells on the PVDF/BTO composite film before and after 20 s of ultrasound. To the right of each group is enlarged view of white circle. Scale bar = 500 and 25 μm . (b) Live/dead staining results of rbMSCs on the piezoelectric films before and after cell harvesting (the top row). Representative live/dead assay of cell sheet harvested immediately and after 2 h (the bottom row). Scale bar = 250 μm . (c) Schematic illustration of the piezoelectricity-induced cell detachment. (d) Cytoskeleton staining of detached rbMSCs and NIH3T3. Scale bar = 250 μm . (e) Ultrasound-induced piezoelectricity affected the paxillin located at the marginal region of the detached cells at the single-cell level and cell-sheet level. Scale bar = 250 μm . (f, g) DNA content reflecting cell number via PicoGreen assay in rbMSCs and NIH3T3 sheet compared with cell culture on TCP at day 1 to 5 ($n=3$).

These results strongly indicated that the piezoelectricity-induced cell harvesting under low-power US is an efficient, universal, and noninvasive pathway. It can be developed as an alternative and show promising in replenishing existing tissue engineering, cell therapy, and build scaffold-free 3D tissue-like constructs.

4. Conclusion

In conclusion, we have fabricated a series of piezoelectric composite films composed of PVDF and BTO NPs with different BTO contents. A 15 wt% doping of PVDF/BTO film exhibited the highest mechanical-electrical conversion capacity and proper mechanical property for cell harvesting. The ultrasound-triggered piezoelectricity led to the conformational change of the adsorbed FN protein, thus changing the adhesion force at the interface between the cells and the composite films. By utilizing the piezoelectric films under remote ultrasound stimulation, both stem cell and fibroblast cell sheets were noninvasively harvested without damaging their viability and proliferation capacity. This work provides an innovative approach for the construction of intact cell sheet without negative damage and exploits a new applicable direction for the further development of piezoelectric materials in biomedical field. Further work will deeply focus on how to refine material performance to achieve more precise cell harvesting and exploring multifunctions of harvested cell sheets.

Declaration of Competing Interest

The authors declare that they have no known competing financial interests or personal relationships that could have appeared to influence the work reported in this paper.

CRediT authorship contribution statement

Xingyi Wan: Investigation, Methodology, Software, Validation, Data curation, Formal analysis, Writing – original draft. **Xiaodi Zhang:** Software, Methodology, Data curation. **Zhirong Liu:** Methodology. **Jiaming Zhang:** Methodology. **Zhou Li:** Supervision, Resources. **Zhong Lin Wang:** Supervision, Resources, Writing – review & editing. **Linlin Li:** Supervision, Conceptualization, Resources, Project administration, Funding acquisition, Writing – review & editing.

Acknowledgements

The work was supported by the National Key R&D project from Minister of Science and Technology, China (2016YFA0202703), the National Nature Science Foundation (No. 82072065, and 81471784), the Nature Science Foundation of Beijing (2172058), and the National Youth Talent Support Program.

Supplementary materials

Supplementary material associated with this article can be found, in the online version, at doi:10.1016/j.apmt.2021.101218.

Reference

- [1] T.L. Downing, J. Soto, C. Morez, T. Houssin, A. Fritz, F. Yuan, J. Chu, S. Patel, D.V. Schaffer, S. Li, Biophysical regulation of epigenetic state and cell reprogramming, *Nat. Mater.* 12 (12) (2013) 1154–1162.
- [2] L. Zhang, Z. Wang, J. Das, M. Labib, S. Ahmed, E.H. Sargent, S.O. Kelley, Potential-Responsive Surfaces for Manipulation of Cell Adhesion, Release, and Differentiation, *Angew. Chem. Int. Ed. Engl.* 58 (41) (2019) 14519–14523.
- [3] T. Panciera, A. Citron, D. Di Biagio, G. Battilana, A. Gandin, S. Giullitti, M. Forcato, S. Bicciato, V. Panzetta, S. Fusco, L. Azolin, A. Totaro, A.P. Dei Tos, M. Fasan, V. Vindigni, F. Bassetto, A. Rosato, G. Brusatin, M. Cordenonsi, S. Piccolo, Reprogramming normal cells into tumour precursors requires ECM stiffness and oncogene-mediated changes of cell mechanical properties, *Nat. Mater.* 19 (2020) 797–806.
- [4] M. Rahmati, E.A. Silva, J.E. Reseland, A.H. C. H.J. Haugen, Biological responses to physicochemical properties of biomaterial surface, *Chem. Soc. Rev.* 49 (2020) 5178–5224.
- [5] B. Wildt, D. Wirtz, P.C. Searson, Programmed subcellular release for studying the dynamics of cell detachment, *Nat. Methods* 6 (3) (2009) 211–213.
- [6] B.S. Kim, M.K. Kim, Y. Cho, E.E. Hamed, M.U. Gillette, H. Cha, N. Miljkovic, V.K. Aakalu, K. Kang, K.N. Son, K.M. Schachtschneider, L.B. Schook, C. Hu, G. Popescu, Y. Park, W.C. Ballance, S. Yu, S.G. Im, J. Lee, C.H. Lee, H. Kong, Electrothermal soft manipulator enabling safe transport and handling of thin cell/tissue sheets and bioelectronic devices, *Sci. Adv.* 6 (42) (2020) eabc5630.
- [7] J.-K. Yoon, M. Misra, S.J. Yu, H.Y. Kim, S.H. Bhang, S.Y. Song, J.-R. Lee, S. Ryu, Y.W. Cho, G.-J. Jeong, S.P. Kwon, S.G. Im, T.I. Lee, B.-S. Kim, Thermosensitive, Stretchable, and Piezoelectric Substrate for Generation of Myogenic Cell Sheet Fragments from Human Mesenchymal Stem Cells for Skeletal Muscle Regeneration, *Adv. Funct. Mater.* 27 (48) (2017) 1703853.
- [8] I. Jun, S.J. Kim, J.-H. Lee, Y.J. Lee, Y.M. Shin, E. Choi, K.M. Park, J. Park, K.D. Park, H. Shin, Transfer Printing of Cell Layers with an Anisotropic Extracellular Matrix Assembly using Cell-Interactive and Thermosensitive Hydrogels, *Adv. Funct. Mater.* 22 (19) (2012) 4060–4069.
- [9] J. Baek, Y. Cho, H.J. Park, G. Choi, J.S. Lee, M. Lee, S.J. Yu, S.W. Cho, E. Lee, S.G. Im, A Surface-Tailoring Method for Rapid Non-Thermosensitive Cell-Sheet Engineering via Functional Polymer Coatings, *Adv. Mater.* 32 (16) (2020) e1907225.
- [10] I. Jun, T. Ahmad, S. Bak, J.Y. Lee, E.M. Kim, J. Lee, Y.B. Lee, H. Jeong, H. Jeon, H. Shin, Spatially Assembled Bilayer Cell Sheets of Stem Cells and Endothelial Cells Using Thermosensitive Hydrogels for Therapeutic Angiogenesis, *Adv. Healthcare Mater.* 6 (9) (2017) 1601340.
- [11] W. Zhang, G. Yang, X. Wang, L. Jiang, F. Jiang, G. Li, Z. Zhang, X. Jiang, Magnetically Controlled Growth-Factor-Immobilized Multilayer Cell Sheets for Complex Tissue Regeneration, *Adv. Mater.* 29 (43) (2017) 1703795.
- [12] S.R. Shin, B. Migliori, B. Miccoli, Y.C. Li, P. Mostafalu, J. Seo, S. Mandla, A. Enrico, S. Antona, R. Sabarish, T. Zheng, L. Pirrami, K. Zhang, Y.S. Zhang, K.T. Wan, D. Demarchi, M.R. Dokmeici, A. Khademhosseini, Electrically Driven Microengineered Bioinspired Soft Robots, *Adv. Mater.* 30 (10) (2018) 1704189.
- [13] Z. Ming, X. Ruan, C. Bao, Q. Lin, Y. Yang, L. Zhu, Micropatterned Protein for Cell Adhesion through Phototriggered Charge Change in a Polyvinylpyrrolidone Hydrogel, *Adv. Funct. Mater.* 27 (25) (2017) 1606258.
- [14] H. Kang, H.J. Jung, S.K. Kim, D.S.H. Wong, S. Lin, G. Li, V.P. Dravid, L. Bian, Magnetic Manipulation of Reversible Nanocaging Controls In Vivo Adhesion and Polarization of Macrophages, *ACS Nano* 12 (6) (2018) 5978–5994.
- [15] A. Sutton, T. Shirman, J.V. Timonen, G.T. England, P. Kim, M. Kolte, T. Ferrante, L.D. Zarzar, E. Strong, J. Aizenberg, Photothermally triggered actuation of hybrid materials as a new platform for in vitro cell manipulation, *Nat. Commun.* 8 (2017) 14700.
- [16] J. Na, J.S. Heo, M. Han, H. Lim, H.O. Kim, E. Kim, Harvesting of Living Cell Sheets by the Dynamic Generation of Diffractive Photothermal Pattern on PEDOT, *Adv. Funct. Mater.* 27 (10) (2017) 1604260.
- [17] J. Jing, S. Chen, Q. Lu, Gradient Photothermal Field for Precisely Directing Cell Sheet Detachment, *Adv. Biosyst.* 3 (5) (2019) e1800334.
- [18] L. Zwi-Dantsis, B. Wang, C. Marjion, S. Zonetti, A. Ferrini, L. Massi, D.J. Stuckey, C.M. Terracciano, M.M. Stevens, Remote Magnetic Nanoparticle Manipulation Enables the Dynamic Patterning of Cardiac Tissues, *Adv. Mater.* 32 (6) (2020) e1904598.
- [19] K.M. Persson, R. Karlsson, K. Svennersten, S. Loffler, E.W. Jager, A. Richter-Dahlfors, P. Konradsson, M. Berggren, Electronic control of cell detachment using a self-doped conducting polymer, *Adv. Mater.* 23 (38) (2011) 4403–4408.
- [20] M. Marzocchi, I. Gualandi, M. Calienni, I. Zironi, E. Scavetta, G. Castellani, B. Fraboni, Physical and Electrochemical Properties of PEDOT:PSS as a Tool for Controlling Cell Growth, *ACS Appl. Mater. Interfaces* 7 (32) (2015) 17993–18003.
- [21] I.C. Peng, C.C. Yeh, Y.T. Lu, S. Muduli, Q.D. Ling, A.A. Alarfaj, M.A. Munusamy, S.S. Kumar, K. Murugan, H.C. Lee, Y. Chang, A. Higuchi, Continuous harvest of stem cells via partial detachment from thermoresponsive nanobrush surfaces, *Biomaterials* 76 (2016) 76–86.
- [22] A.M. Wan, R.M. Schur, C.K. Ober, C. Fischbach, D. Gourdon, G.G. Malliaras, Electrical control of protein conformation, *Adv. Mater.* 24 (18) (2012) 2501–2505.
- [23] A.P. Kalra, B.B. Eakins, S.D. Patel, G. Ciniero, V. Rezanian, K. Shankar, J.A. Tuszynski, All Wired Up: An Exploration of the Electrical Properties of Microtubules and Tubulin, *ACS Nano* 14 (12) (2020) 16301–16320.
- [24] S. Jain, A. Sharma, B. Basu, Vertical electric field stimulated neural cell functionality on porous amorphous carbon electrodes, *Biomaterials* 34 (37) (2013) 9252–9263.
- [25] G. Thirivikraman, G. Madras, B. Basu, Electrically driven intracellular and extracellular nanomanipulators evoke neurogenic/cardiomyogenic differentiation in human mesenchymal stem cells, *Biomaterials* 77 (2016) 26–43.
- [26] P. Yu, C. Ning, Y. Zhang, G. Tan, Z. Lin, S. Liu, X. Wang, H. Yang, K. Li, X. Yi, Y. Zhu, C. Mao, Bone-Inspired Spatially Specific Piezoelectricity Induces Bone Regeneration, *Theranostics* 7 (13) (2017) 3387–3397.
- [27] K. Kapat, Q.T.H. Shubhra, M. Zhou, S. Leeuwenburgh, Piezoelectric Nano-Biomaterials for Biomedicine and Tissue Regeneration, *Adv. Funct. Mater.* 30 (2020) 1909045.
- [28] Y. Su, C. Chen, H. Pan, Y. Yang, G. Chen, X. Zhao, W. Li, Q. Gong, G. Xie, Y. Zhou, S. Zhang, H. Tai, Y. Jiang, J. Chen, Muscle Fibers Inspired High-Performance Piezoelectric Textiles for Wearable Physiological Monitoring, *Adv. Funct. Mater.* (2021) 2010962.
- [29] M.T. Chorsi, E.J. Curry, H.T. Chorsi, R. Das, J. Baroody, P.K. Purohit, H. Ilies, T.D. Nguyen, Piezoelectric Biomaterials for Sensors and Actuators, *Adv. Mater.* 31 (1) (2019) e1802084.
- [30] T. Li, Z.Q. Feng, M. Qu, K. Yan, T. Yuan, B. Gao, T. Wang, W. Dong, J. Zheng, Core/Shell Piezoelectric Nanofibers with Spatial Self-Orientated beta-Phase Nanocrystals for Real-Time Micropressure Monitoring of Cardiovascular Walls, *ACS Nano* 13 (9) (2019) 10062–10073.
- [31] X. Zhang, X. Cui, D. Wang, S. Wang, Z. Liu, G. Zhao, Y. Zhang, Z. Li, Z.L. Wang, L. Li, Piezoelectric Nanotopography Induced Neuron-Like Differentiation of Stem Cells, *Adv. Funct. Mater.* 29 (22) (2019) 1900372.
- [32] L. Liu, B. Chen, K. Liu, J. Gao, Y. Ye, Z. Wang, N. Qin, D.A. Wilson, Y. Tu, F. Peng, Wireless Manipulation of Magnetic/Piezoelectric Micromotors for Precise Neural Stem-Like Cell Stimulation, *Adv. Funct. Mater.* 30 (11) (2020) 1910108.
- [33] J.K. Yoon, T.I. Lee, S.H. Bhang, J.Y. Shin, J.M. Myoung, B.S. Kim, Stretchable Piezoelectric Substrate Providing Pulsatile Mechanoelectric Cues for Cardiomyogenic Differentiation of Mesenchymal Stem Cells, *ACS Appl. Mater. Interfaces* 9 (27) (2017) 22101–22111.
- [34] A. Marino, G.G. Genchi, E. Sinibaldi, G. Ciofani, Piezoelectric Effects of Materials on Bio-Interfaces, *ACS Appl. Mater. Interfaces* 9 (21) (2017) 17663–17680.
- [35] N. Barroca, P.M. Vilarinho, A.L. Daniel-da-Silva, A. Wu, M.H. Fernandes, A. Gruber, Protein adsorption on piezoelectric poly(L-lactic) acid thin films by scanning probe microscopy, *Appl. Phys. Letters* 98 (13) (2011).
- [36] G.G. Genchi, A. Marino, A. Rocca, V. Mattoli, G. Ciofani, Barium titanate nanoparticles: promising multitasking vectors in nanomedicine, *Nanotechnology* 27 (23) (2016) 232001.
- [37] K. Shi, B. Chai, H. Zou, P. Shen, B. Sun, P. Jiang, Z. Shi, X. Huang, Interface induced performance enhancement in flexible BaTiO₃/PVDF-TrFE based piezoelectric nanogenerators, *Nano Energy* 80 (2021) 105515.
- [38] A. Micsonai, F. Wien, L. Kernya, Y.H. Lee, Y. Goto, M. Refregiers, J. Kardos, Accurate secondary structure prediction and fold recognition for circular dichroism spectroscopy, *Proc. Natl. Acad. Sci. U. S. A.* 112 (24) (2015) E3095–E3103.
- [39] A. Micsonai, F. Wien, E. Bulyaki, J. Kun, E. Moussong, Y.H. Lee, Y. Goto, M. Refregiers, J. Kardos, BeStSel: a web server for accurate protein secondary structure prediction and fold recognition from the circular dichroism spectra, *Nucleic Acids Res* 46 (W1) (2018) W315–W322.
- [40] X. Zhang, J. Nie, X. Yang, Z. Liu, W. Guo, J. Qiu, S. Wang, X. Yu, Y. Guan, H. Liu, L. Li, Nanostructured molybdenum disulfide biointerface for adhesion and osteogenic differentiation of mesenchymal stem cells, *Appl. Mater. Today* 10 (2018) 164–172.
- [41] W. Guo, X. Zhang, X. Yu, S. Wang, J. Qiu, W. Tang, L. Li, H. Liu, Z.L. Wang, Self-Powered Electrical Stimulation for Enhancing Neural Differentiation of Mesenchymal Stem Cells on Graphene-Poly(3,4-ethylenedioxythiophene) Hybrid Microfibers, *ACS Nano* 10 (5) (2016) 5086–5095.
- [42] C.D. Reyes, A.J. Garcia, A centrifugation cell adhesion assay for high-throughput screening of biomaterial surfaces, *J. Biomed. Mater. Res. A* 67 (1) (2003) 328–333.
- [43] P. Zhu, Y. Chen, J. Shi, Piezocatalytic Tumor Therapy by Ultrasound-Triggered and BaTiO₃-Mediated Piezoelectricity, *Adv. Mater.* 32 (29) (2020) e2001976.
- [44] C. Pan, J. Zhai, Z.L. Wang, Piezotronics and Piezo-phototronics of Third Generation Semiconductor Nanowires, *Chem. Rev.* 119 (15) (2019) 9303–9359.
- [45] J. Wu, Q. Xu, E. Lin, B. Yuan, N. Qin, S.K. Thatikonda, D. Bao, Insights into the Role of Ferroelectric Polarization in Piezocatalysis of Nanocrystalline BaTiO₃, *ACS Appl. Mater. Interfaces* 10 (21) (2018) 17842–17849.
- [46] G.G. Genchi, L. Ceseracciu, A. Marino, M. Labardi, S. Marras, F. Pignatelli, L. Bruschini, V. Mattoli, G. Ciofani, P(VDF-TrFE)/BaTiO₃ Nanoparticle Composite Films Mediate Piezoelectric Stimulation and Promote Differentiation of SH-SY5Y Neuroblastoma Cells, *Adv. Healthcare Mater.* 5 (14) (2016) 1808–1820.
- [47] I. Cockerill, Y. Su, J.H. Lee, D. Berman, M.L. Young, Y. Zheng, D. Zhu, Micro-/Nano-Topography on Bioresorbable Zinc Dictates Cytocompatibility, Bone Cell Differentiation, and Macrophage Polarization, *Nano Lett* (2020) 4594–4602.
- [48] C. Zhang, W. Liu, C. Cao, F. Zhang, Q. Tang, S. Ma, J. Zhao, L. Hu, Y. Shen, L. Chen, Modulating Surface Potential by Controlling the beta Phase Content in Poly(vinylidene fluoride)trifluoroethylene Membranes Enhances Bone Regeneration, *Adv. Healthcare Mater.* 7 (11) (2018) e1701466.
- [49] M. El Achaby, F.Z. Arrakhiz, S. Vaudreuil, E.M. Essassi, A. Qaiss, Piezoelectric β -polymorph formation and properties enhancement in graphene

- oxide-PVDF nanocomposite films, *Appl. Surf. Sci.* 258 (19) (2012) 7668–7677.
- [50] C.F. Guimarães, L. Gasperini, A.P. Marques, R.L. Reis, The stiffness of living tissues and its implications for tissue engineering, *Nat. Rev. Mater.* 5 (5) (2020) 351–370.
- [51] X. Zhang, C. Zhang, Y. Lin, P. Hu, Y. Shen, K. Wang, S. Meng, Y. Chai, X. Dai, X. Liu, Y. Liu, X. Mo, C. Cao, S. Li, X. Deng, L. Chen, Nanocomposite Membranes Enhance Bone Regeneration Through Restoring Physiological Electric Microenvironment, *ACS Nano* 10 (8) (2016) 7279–7286.
- [52] C. Shuai, G. Liu, Y. Yang, F. Qi, S. Peng, W. Yang, C. He, G. Wang, G. Qian, A strawberry-like Ag-decorated barium titanate enhances piezoelectric and antibacterial activities of polymer scaffold, *Nano Energy* 74 (2020) 104825.
- [53] P. Kanchanawong, G. Shtengel, A.M. Pasapera, E.B. Ramko, M.W. Davidson, H.F. Hess, C.M. Waterman, Nanoscale architecture of integrin-based cell adhesions, *Nature* 468 (7323) (2010) 580–584.
- [54] X. Jia, K. Minami, K. Uto, A.C. Chang, J.P. Hill, J. Nakanishi, K. Ariga, Adaptive Liquid Interfacially Assembled Protein Nanosheets for Guiding Mesenchymal Stem Cell Fate, *Adv. Mater.* 32 (4) (2020) e1905942.
- [55] H. Bachman, J. Nicosia, M. Dysart, T.H. Barker, Utilizing Fibronectin Integrin-Binding Specificity to Control Cellular Responses, *Adv. Wound Care (New Rochelle)* 4 (8) (2015) 501–511.
- [56] J.R. Brennan, D.C. Hocking, Cooperative effects of fibronectin matrix assembly and initial cell-substrate adhesion strength in cellular self-assembly, *Acta Biomater* 32 (2016) 198–209.
- [57] N.A. Dzhoyashvili, K. Thompson, A.V. Gorelov, Y.A. Rochev, Film Thickness Determines Cell Growth and Cell Sheet Detachment from Spin-Coated Poly(N-Isopropylacrylamide) Substrates, *ACS Appl. Mater. Interfaces* 8 (41) (2016) 27564–27572.
- [58] E. Osterlund, I. Eronen, K. Osterlund, M. Vuento, Secondary structure of human plasma fibronectin: conformational change induced by calf alveolar heparan sulfates, *Biochemistry* 24 (11) (1985) 2661–2667.
- [59] N.E. Muzzio, M.A. Pasquale, X. Rios, O. Azzaroni, J. Llop, S.E. Moya, Adsorption and Exchangeability of Fibronectin and Serum Albumin Protein Corona on Annealed Polyelectrolyte Multilayers and Their Consequences on Cell Adhesion, *Adv. Mater. Interfaces* 6 (8) (2019) 1900008.
- [60] B. Tang, J. Zhuang, L. Wang, B. Zhang, S. Lin, F. Jia, L. Dong, Q. Wang, K. Cheng, W. Weng, Harnessing Cell Dynamic Responses on Magnetolectric Nanocomposite Films to Promote Osteogenic Differentiation, *ACS Appl. Mater. Interfaces* 10 (9) (2018) 7841–7851.
- [61] A. Elosegui-Artola, X. Trepast, P. Roca-Cusachs, Control of Mechanotransduction by Molecular Clutch Dynamics, *Trends Cell Biol* 28 (5) (2018) 356–367.
- [62] J.D. Humphrey, E.R. Dufresne, M.A. Schwartz, Mechanotransduction and extracellular matrix homeostasis, *Nat. Rev. Mol. Cell Biol.* 15 (12) (2014) 802–812.
- [63] T.S. Stappenbeck, H. Miyoshi, The role of stromal stem cells in tissue regeneration and wound repair, *Science* 324 (5935) (2009) 1666–1669.
- [64] Y. Kfoury, D.T. Scadden, Mesenchymal cell contributions to the stem cell niche, *Cell Stem Cell* 16 (3) (2015) 239–253.